

Object Agnostic 3D Lifting in Space and Time

Christopher Fusco
The University of Adelaide

christopher.fusco@adelaide.edu.au

Mosam Dabhi
Carnegie Mellon University

Shin-Fang Ch'ng
The University of Adelaide

Simon Lucey
The University of Adelaide

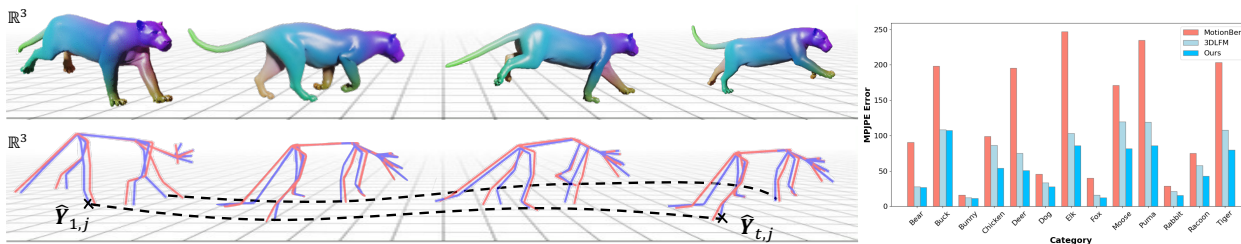


Figure 1. Left: Bottom row shows the predicted 3D skeletons of a puma category in motion. The blue sticks represent our model’s predictions, closely tracking the red ground-truth positions, showing our model’s ability to generate smooth and precise motion over time. The dashed line highlights the trajectory of a specific joint $\hat{Y}_{t,j}$, emphasizing the temporal consistency and accuracy of our approach. Right: Quantitative SA-MPIPE comparison across 13 animal categories, where our method consistently outperforms competing models.

Abstract

We present a spatio-temporal perspective on category-agnostic 3D lifting of 2D keypoints over a temporal sequence. Our approach differs from existing state-of-the-art methods that are either: (i) object agnostic, but can only operate on individual frames, or (ii) can model space-time dependencies, but are only designed to work with a single object category. Our approach is grounded in two core principles. First, when there is a lack of data about an object, general information from similar objects can be leveraged for better performance. Second, while temporal information is important, the most critical information is in immediate temporal proximity. These two principles allow us to outperform current state-of-the-art methods on per-frame and per-sequence metrics for a variety of objects. Lastly, we release a new synthetic dataset containing 3D skeletons and motion sequences of a diverse set of animals. Dataset and code will be made publicly available.

1. Introduction

Reconstructing 3D deforming objects from 2D landmarks is a long-standing challenge in computer vision. While traditional approaches use multiple camera views to mitigate ambiguities, recent learning-based methods are capable of lifting 3D object structure using sparse 2D keypoints from a single camera. Coupled with an abundance of publicly available 3D human pose data, human-specific lifting models like MotionBERT [34] have become increasingly capable. However, their reliance on human-specific information and vast amounts of training data make it problematic if they are to be used for other objects. In particular, animals pose a significant challenge due to the limited amount of publicly available 3D animal data.

This has motivated recent developments around object-agnostic lifting. Most notably, 3D-LFM [7] achieved state-of-the-art lifting performance by leveraging a combined dataset of various object categories. It leverages the permutation equivariant property of transformers, along with additional inductive biases, to handle object category imbalance and within-category object rig/skeleton variation. However, a shortfall of 3D-LFM is its inability to utilize

temporal information, leading to less accurate reconstructions in dynamic sequences.

Our work tackles these challenges by introducing the first object-agnostic 3D lifting framework that is both data-efficient and temporally aware. Our approach uses the power of transformers with a strategic inductive bias that focuses on temporally proximate frames, enabling it to capture motion dynamics effectively. This approach improves the accuracy of 3D reconstructions across various object categories, even in scenarios with limited data and unseen objects. Additionally, we address the lack of publicly available datasets for diverse animal skeletons and motion sequences by creating a new synthetic dataset. This dataset includes 4D labels for 13 animal categories, encompassing 698 animation sequences with temporal consistency, designed to foster further research in class-agnostic lifting.

The contributions of this paper are:

- We propose a class-agnostic lifting model with a strategic inductive bias directly embedded in the architecture. We demonstrate the state-of-the-art 3D lifting of our approach across scenarios involving noise, occlusions, and unseen objects.
- We contribute a new synthetic dataset containing 4D skeletons for a variety of animals with animated behaviour sequences, where temporal consistency is prioritised through a non-linear refinement procedure.

We empirically validate the effectiveness of our approach on our synthetic dataset. We achieve state-of-the-art results with existing metrics and provide an additional metric to provide a more complete analysis. We plan to release all dataset and code.

2. Related Works

2.1. 3D Pose Estimation

Obtaining the 3D pose of an object from a single monocular camera generally follows one of two paths. The first approach directly predicts the 3D pose from RGB images [2, 22, 25, 26], but this method often struggles with generalization to distribution shifts, such as varying lighting and background conditions. Alternatively, a two-stage method divides the task between two specialized models [3, 4, 11, 20]: a pose detector first extracts the 2D pose, which is then lifted into 3D by a separate model. Our work aligns with this two-stage approach, focusing on improving the robustness and generalization of the 3D lifting step.

2.2. Object-Specific Lifting

Traditional non-rigid structure-from-motion (NRSfM) algorithms have been effective for modeling simple objects, such as human bodies and hands [5, 9]. These methods rely on the availability of 2D keypoints and specific 3D supervision for the object in question. However, recent

deep learning approaches have demonstrated superior performance in handling the complexity of various object rigs [13, 17, 24, 28]. Despite these advancements, they still require the 2D keypoints to have consistent semantic correspondence across all instances of the object, meaning that a specific landmark, such as an elbow, must have the same semantic meaning across different poses.

This limitation persists even in state-of-the-art deep learning models like MotionBERT [34] and others [3, 4], which are tailored specifically for human body 3D lifting. The specialized nature of these models and their dependency on large datasets make them unsuitable for objects with limited available data, such as animals. Animal-specific 3D lifting models suffer from similar issues, often being restricted to a single animal category and demonstrating poor generalization due to data scarcity [10, 15, 21].

2.3. Object-Agnostic Lifting

The paradigm of object-agnostic lifting has been recently pioneered by 3D-LFM [7], which can handle a wide range of object categories by leveraging large-scale information of large-scale data to enhance performance for underrepresented or unseen objects. However, unlike object-specific models like Motionbert [34], 3D-LFM does not incorporate temporal information, which is needed for accurate 3D reconstruction over sequences. Our framework builds upon this insight, integrating the strengths of both object-agnostic lifting and temporal modeling to achieve improved results.

2.4. Animal Datasets

To effectively benchmark category-agnostic lifting over videos of animals, a diverse set of animal categories with accurately labeled 3D skeletons is essential. Recent animal datasets have made strides in this area but are often limited to single atemporal images [29, 31], with few publicly available datasets offering 3D poses of animals in video sequences [6, 18]. Moreover, methods to collect data for a broad set of animals are typically impractical, expensive, or yield noisy results.

Inspired by the tracking community, we turn to synthetic data [8, 14, 33]. Existing synthetic datasets are often restricted to a single animal, such as pigs [1] or ants [27], and generally contain only simplistic motion sequences. The DeformableThings4D [19] dataset offers more complex and diverse motion sequences animated by artists, but it was created for dense mesh recovery and does not include 3D skeletons. We build upon these models and animations to create a new dataset specifically designed for the task of class-agnostic 3D lifting.

3. Method

In this section we explain our data collection pipeline and class-agnostic lifting model.

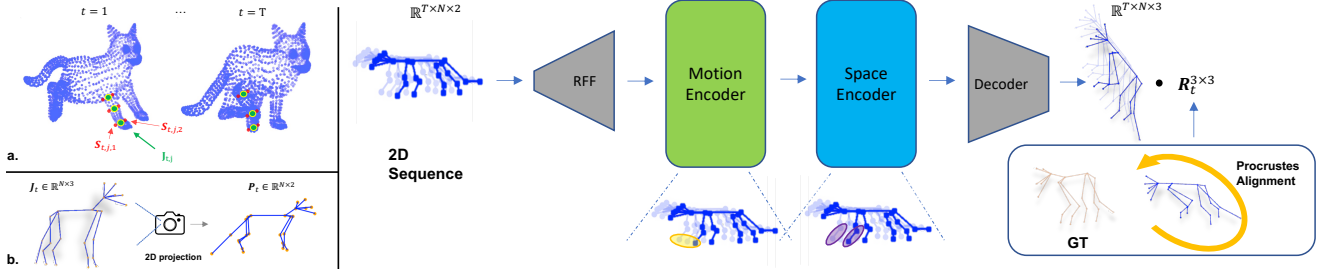


Figure 2. **Overview of our data pipeline and 3D lifting model.** The left side of the figure demonstrates (a) the process of calculating joints from animal mesh vertices, and (b) the projection of the skeleton joints into 2D keypoints. The right side of the figure illustrates our lifting model at a high-level. The sequence of 2D input and temporal index is projected and passed through our motion encoder and space encoder layers. The spatio-temporal latent features are decoded into canonical 3D structures. The canonical structures are then aligned to the ground truth (GT) via procrustes-alignment for calculating the loss.

3.1. Dataset

We find a noticeable gap in available public datasets containing diverse 3D animal skeletons with realistic motion sequences. We aim to fill this gap by creating a new synthetic dataset building on the mesh vertices and animation sequences provided by the DeformableThings4D [19] dataset. We provide 3D skeleton labels for 13 animal categories, totalling 698 animation sequences with temporal correspondence across 51,360 frames. We provide statistics and examples of our dataset in the supp. material. We detail our data collection pipeline in following section, see Fig. 2 for a visualization of our data collection pipeline.

3.1.1 Animal joints

Given the vertices of a skin-tight mesh of an animal and an associated sequence of movement, our aim is to find the 3D locations of anatomically-accurate skeleton joints of the animal. We define the locations of K vertices and N joints in 3D space throughout a sequence of T frames as $\mathbf{V} \in \mathbb{R}^{T \times K \times 3}$ and $\mathbf{J} \in \mathbb{R}^{T \times N \times 3}$, respectively. Note that the number of mesh vertices, joints, and frames may vary across animals and sequences. We take inspiration from motion capture, where markers are attached to an object and used to estimate joint positions via triangulation. Let us define $j \in \{1, 2, \dots, N\}$. We strategically select a subset of vertices $\mathbf{S}_{t,j} = \{\mathbf{S}_{t,j,1}, \dots, \mathbf{S}_{t,j,m}\} \subset \mathbf{V}_t$ to be virtual markers, such that the mean of the virtual markers will provide the location of a joint j in frame t :

$$\mathbf{J}_{t,j} = \frac{1}{m} \sum_{i=1}^m \mathbf{S}_{t,j,i}. \quad (1)$$

The selection of vertices for a subset $\mathbf{S}_{t,j}$ is guided by a visual inspection of $\mathbf{J}_{t,j}$ and the motion similarity of vertices within $\mathbf{S}_{t,j}$. The bones of the animal are defined as an adjacency matrix $\mathbf{A}^{N \times N}$ containing the connections be-

tween joints. We decide the number of joints, their approximate locations, and their connections by reviewing the anatomical structure of the target animal.

3.1.2 Non-linear optimisation

The noise that is inherently present in our human annotation process occasionally results in the length of animal bones to change over time, measured as the Euclidean distance between two connected joints. We adopt an additional inverse-kinematics optimisation to refine the position of joints such that the bone lengths are consistent. We formulate the problem as solving for the pose angles $\theta \in \mathbb{R}^{T \times N \times 3}$ of forward kinematics for each joint j in frame t :

$$\hat{\mathbf{J}}_{t,j} = f(\theta_{t,j}) = f(\theta_{t,p}) \cdot \begin{bmatrix} \mathcal{R}(\theta_{t,j}) & \mathbf{L}_{j,p} \\ \mathbf{0} & \mathbf{1} \end{bmatrix}, \quad (2)$$

where p is the parent of joint j in the kinematic chain, \mathcal{R} transforms $\theta_{t,j}$ into a valid $\mathbf{R} \in SO(3)$ rotation matrix using Rodrigues' rotation formula, and $\mathbf{L}_{j,p}$ is the bone length between joints j and p in the first frame. Forcing the \mathbf{L} translation vector to be from a single frame forces bone lengths to be the same for every frame.

We use gradient descent to optimise the objective function

$$\text{minimize}_{\theta} \sum_{t=1}^T \sum_{j=1}^N \left\| \hat{\mathbf{J}}_{t,j} - \mathbf{J}_{t,j} \right\|_2 + \lambda L_S, \quad (3)$$

where L_S is an additional smoothness regulariser:

$$L_S = \left\| \hat{\mathbf{J}}_{t,j} - \hat{\mathbf{J}}_{t-1,j} \right\|_2. \quad (4)$$

Our inverse-kinematics optimisation provides a new set of joints $\hat{\mathbf{J}}_{t,j}$ ensuring that an animal has consistent bone lengths throughout any complex sequence of movement.

3.1.3 Perspective projection

We define an initial camera pose to satisfy two conditions. The mean location of the animal throughout the sequence is at the center of the camera view, and all joints are within view for the entirety of the sequence. We randomly rotate the camera around the y -axis and then project the points to the 2D camera plane. For our purpose we do this only once for each animation sequence, however this process can be used to obtain many different views of the animal throughout the sequence.

3.2. Lifting model

Given an input sequence of 2D skeletons $\mathbf{X} \in \mathbb{R}^{T \times J \times 2}$, where T is the number of frames in the video and J the number of joints, our goal is to reconstruct the 3D skeletons $\hat{\mathbf{Y}} \in \mathbb{R}^{T \times J \times 3}$ of the object for each frame.

3.2.1 Keypoint features

The attention mechanism of transformers is inherently permutation equivariant, such that inputs can be randomly permuted and the corresponding outputs will remain the same. We leverage this property to handle objects with different joint configurations. We utilise the masking mechanism of [7] to handle the technical challenge of training with different numbers of joints. Inputs are zero-padded up to the maximum number of joints in a mini-batch and a mask $\mathbf{M} \in \{0, 1\}^J$ is used to ignore padded joints. Each element in \mathbf{M} is defined as:

$$\mathbf{M}_i = \begin{cases} 1 & \text{if joint } i \text{ is present} \\ 0 & \text{otherwise} \end{cases} \quad (5)$$

We project the 2D skeletons to D -dimensional features $\mathbf{F} \in \mathbb{R}^{T \times J \times D}$ using Random Fourier Features (RFF) [32]. We additionally encode each 2D joint (x, y) with its temporal location t in the video. We compute the feature of an input $\mathbf{p} = [x, y, t]^T$ as:

$$\phi(\mathbf{p}) = \sqrt{\frac{2}{D}} \left[\sin(\mathbf{W} \cdot \mathbf{p} + \mathbf{b}); \cos(\mathbf{W} \cdot \mathbf{p} + \mathbf{b}) \right], \quad (6)$$

where $\mathbf{W} \in \mathbb{R}^{\frac{D}{2} \times 3}$ is sampled from a normal distribution $\mathcal{N}(0, I)$ and $\mathbf{b} \in \mathbb{R}^{\frac{D}{2}}$ is sampled from a uniform distribution $\mathcal{U}(0, \frac{1}{2\pi})$. We choose analytical RFF for its success in low-data and out-of-distribution (OOD) scenarios [7, 32]. We find that encoding the temporal position is beneficial for our motion encoder.

3.2.2 Motion encoder

Our motion encoder leverages multi-head self-attention (MHSA) to embed temporal context into the keypoint fea-

tures. Although we choose MHSA for its ability to use information from all frames, its lack of any inductive bias makes it unsuitable for tasks with limited data. We argue that it is not necessary to consider all frames in a sequence because most of the useful information can be found in nearby frames. We explicitly impose this inductive bias into the MHSA blocks by applying a binary mask to the intermediate attention maps. We define the mask $\mathbf{Z} \in \mathbb{R}^{T \times T}$ for a joint at time t as:

$$\mathbf{Z}_{t,i} = \begin{cases} 1 & \text{for } t - \alpha \leq i \leq t + \alpha \\ 0 & \text{otherwise} \end{cases} \quad (7)$$

where α is a hyper-parameter controlling the number of frames before and after t that can contribute information during attention..

Given a set of spatial features $\mathbf{F} \in \mathbb{R}^{T \times J \times D}$ as input to our motion encoder, we matrix transpose to get $\mathbf{F}_M \in \mathbb{R}^{J \times T \times D}$. We first apply linear projections to obtain queries \mathbf{Q} , keys \mathbf{K} , and values \mathbf{V} for each head h :

$$\mathbf{Q}^{(h)} = \mathbf{F}\mathbf{W}_Q^{(h)}, \mathbf{K}^{(h)} = \mathbf{F}\mathbf{W}_K^{(h)}, \mathbf{V}^{(h)} = \mathbf{F}\mathbf{W}_V^{(h)}, \quad (8)$$

where $\mathbf{Q}^{(h)}, \mathbf{K}^{(h)}, \mathbf{V}^{(h)} \in \mathbb{R}^{N, T, \frac{D}{H}}$ for a total of H heads. We apply our temporal mask \mathbf{Z} before the non-linear softmax operation for each head:

$$\text{head}_h = \text{softmax}\left(\frac{\mathbf{Q}^{(h)}(\mathbf{K}^{(h)})^T}{\sigma} \times \mathbf{Z}\right) \cdot \mathbf{V}^{(h)}, \quad (9)$$

where σ is a scaling factor. Finally, each head is concatenated and projected:

$$\text{MHSA}_\alpha(\mathbf{F}_M) = [\text{head}_1; \dots; \text{head}_h] \mathbf{W}_P. \quad (10)$$

We follow the standard procedure of applying a residual connection and layer normalisation before obtaining the final output of one windowed-MHSA layer. We stack P of these layers with residual connections to create our motion encoder.

3.2.3 Space encoder

The space encoder uses the features from our motion encoder to model the relationships among joints in a single frame. We found the hybrid graph-based approach of [7] to perform favorably for our task. Given the motion features $\mathbf{F}_M \in \mathbb{R}^{T \times J \times D}$, a single space-layer has two simultaneous processing streams, one for capturing the local connectivity between joints G_{local} , and another for capturing global connectivity G_{global} . These two streams are concatenated and projected to provide an output containing a combination of both streams \mathbf{F}_S as:

$$\mathbf{F}_S = \text{MLP}([G_{\text{local}}(\mathbf{F}_M, \mathbf{A}); G_{\text{global}}(\mathbf{F}_M)]). \quad (11)$$

The local graph-attention G_{local} utilises an adjacency matrix of the joint connections $\mathbf{A} \in \mathbb{R}^{J \times J}$ to model the object connectivity. A layer normalisation and skip connection is applied to give the layer output. As with our motion encoder, we stack O layers with residual connections between them.

3.2.4 Decoder and Procrustes-based loss

Lastly, given the latent features \mathbf{F}_S , we use an MLP to decode these features to obtain the predicted 3D structures $\hat{\mathbf{Y}}^{\text{canon}} \in \mathbb{R}^{T \times J \times 3}$ of the object in a canonical 3D space

$$\hat{\mathbf{Y}}^{\text{canon}} = \text{MLP}(\mathbf{F}_S). \quad (12)$$

We align each canonical prediction $\hat{\mathbf{Y}}^{\text{canon}}$ with the ground truth \mathbf{Y} via a Procrustes alignment method which solves for the optimal rotation $\tilde{\mathbf{R}}_t$ individually for each frame t as:

$$\underset{\mathbf{R}_t \in SO(3)}{\text{minimize}} \left\| \mathbf{Y}_t - \hat{\mathbf{Y}}_t^{\text{canon}} \mathbf{R}_t \right\|_2. \quad (13)$$

In practice, we use Singular Value Decomposition (SVD) to solve this optimisation problem. To ensure that $\tilde{\mathbf{R}}_t$ belongs to the special orthogonal group $SO(3)$, we enforce $\det(\tilde{\mathbf{R}}_t) = +1$. This step is crucial for mitigating reflection ambiguity in our predictions.

The resulting $\tilde{\mathbf{R}}_t$ is used to align our canonical predictions with the ground truth. We additionally scale the predictions relative to the ground truth using a scaling factor $s \in \mathbb{R}^T$:

$$\hat{\mathbf{Y}}_t = s_t \cdot (\hat{\mathbf{Y}}_t^{\text{canon}} \tilde{\mathbf{R}}_t) \quad (14)$$

3.2.5 Loss function

With our predictions now aligned with the ground truth, we can compute our loss. We compute the Mean Squared Error (MSE) of the 3D points along with an additional velocity error \mathcal{L}_{vel} :

$$\mathcal{L}_{\text{total}} = \sum_{t=1}^T \sum_{j=1}^J \left\| \mathbf{Y}_{t,j} - \hat{\mathbf{Y}}_{t,j} \right\|_2 + \lambda \mathcal{L}_{\text{vel}}, \quad (15)$$

$$\mathcal{L}_{\text{vel}} = \sum_{t=2}^T \sum_{j=1}^J \left\| (\mathbf{Y}_{t,j} - \mathbf{Y}_{t-1,j}) - (\hat{\mathbf{Y}}_{t,j} - \hat{\mathbf{Y}}_{t-1,j}) \right\|_2. \quad (16)$$

We use λ as a scalar to weight the velocity loss.

4. Experiments

We evaluate our method on various animal categories to assess its performance and generalisation properties. Comparative analyses are with recent state-of-the-art video (MotionBERT) [34] and single-frame (3D-LFM) lifting models [7]. For completeness, we also include comparisons on human-specific lifting, see the supp. material for results on the Human3.6M benchmark.

Datasets We use a dataset of 13 animals generated with our data pipeline, as described in Sec. 3. The 2D keypoints provided by off-the-shelf pose detectors [30] are inherently noisy due to factors such as lighting conditions and image quality. To simulate these conditions, we synthetically perturb the 2D keypoints with an additive noise, which corresponds to an average 3-pixel error. We present results for non-noisy data in the supp. material. Note that we also provide comparisons on a real-world example, see Fig. 1 and 3D human pose estimation results in the supp. material. We normalise the 2D keypoints and 3D labels to $[-1, 1]$, after scaling the 3D labels following existing works on 3D human pose estimation [34]. We split the data for training by randomly selecting 80% of the animations sequences

for each animal, with the remaining animations withheld for testing. For further information about the data, see Sec. 3.

Evaluation protocols Previous video lifting methods [4, 11, 20, 34] evaluate the non-rigid structure and motion of their method by calculating the mean per-joint position error (MPJPE) directly with the ground truth in the *camera space*. However, our model and 3D-LFM make predictions in a *canonical space* that requires the alignment of each frame to the ground truth. As such, we instead use the standard *per-frame* Procrustes-aligned MPJPE metric and refer to it as the frame-aligned MPJPE (**FA-MPJPE**) for brevity. Additionally, we compose a metric to measure the relative motion error in a video sequence.

Sequence-Aligned MPJPE We formulate the sequence-aligned MPJPE (**SA-MPJPE**) as solving for a *single* rotation matrix $\mathbf{R} \in SO(3)$ to align the 3D predictions $\hat{\mathbf{Y}}$ and ground truth \mathbf{Y} for all T frames in a sequence. This is in contrast to the SA-MPJPE that aligns each individual frame in a sequence by solving for T rotation matrices. After alignment we compute the MSE to produce the final error value. Let us specify $\hat{\mathbf{Y}}, \mathbf{Y} \in \mathbb{R}^{T \times J \times 3}$, for J joints, to define our metric as

$$\underset{\mathbf{R}}{\text{minimize}} \sum_{t=1}^T \left\| \mathbf{Y}_t - \hat{\mathbf{Y}}_t \mathbf{R} \right\|_2. \quad (17)$$

Method	Bear	Buck	Bunny	Chicken	Deer	Dog	Elk	Fox	Moose	Puma	Rabbit	Raccoon	Tiger	Avg
MotionBERT	94.5	208.1	16.7	108.2	200.7	50.1	267.4	40.6	189.2	254.4	30.7	77.4	211.8	134.6
3D-LFM	47.6	158.2	23.2	92.3	156.8	53.9	147.8	22.2	274.7	163.4	37.8	70.0	165.4	108.7
Ours	29.2	128.4	17.1	60.8	57.3	32.8	103.1	14.2	97.9	93.2	19.0	44.5	90.8	60.6
MotionBERT	90.7	198.1	16.0	99.0	195.5	45.8	246.8	39.9	170.9	235.0	28.6	74.9	203.2	126.5
3D-LFM	27.9	108.3	12.2	86.3	75.0	33.3	103.0	16.2	119.7	119.3	21.2	57.6	107.7	68.3
Ours	26.7	107.3	11.2	54.2	50.9	27.9	86.1	12.4	81.6	85.9	15.4	42.8	79.8	52.5
MotionBERT	3.2	11.0	1.1	3.9	6.9	2.6	10.4	1.3	17.8	9.8	2.1	4.0	9.8	6.5
3D-LFM	7.6	29.0	3.4	8.4	26.3	8.4	26.5	3.8	43.4	27.3	6.7	12.3	30.4	18.0
Ours	2.5	12.1	1.3	3.4	5.9	2.9	9.3	1.2	12.5	8.9	2.0	3.6	9.1	5.7

Table 1. **Quantitative comparison of 2D to 3D lifting with 13 animals.** We report, in millimeters, the Sequence-Aligned MPJPE (top), Frame-Aligned MPJPE (middle), and Sequence-Aligned MPVE (bottom), see Sec. 4 for details of these evaluation metrics. Our approach (Ours) outperforms existing state-of-the-arts with significant gap across multiple animal categories.

Method	MC	FA-MPJPE↓	SA-MPJPE↓	SA-MPVE↓
MotionBERT	-	176.0	199.9	9.78
	✓	126.5	134.6	6.5
3D-LFM	-	89.2	126.4	20.5
	✓	68.3	108.7	18.0
Ours	-	105.4	128.4	11.0
	✓	52.5	60.6	5.7

Table 2. **Quantitative comparison between multi-category (MC) and single-category training.** We use a ✓ for models trained with multi-category training. Each method benefits from multi-category training. See supp. material for a breakdown of per-animal results.

Compared to Eq. (13) we are instead solving for only one global \mathbf{R} . Our metric thus captures any error in the motion that occurs between subsequent frames of a sequence.

Lastly, we are able to report the mean per-joint velocity error (commonly referred to as MPVE) after we align the predictions $\hat{\mathbf{Y}}$ to the ground truth for the whole sequence. For clarity in our comparisons, we refer to this as **SA-MPVE**.

Implementation details Here we provide important implementation details of our method and refer the reader to the supp. material for further details. We train on a total of 871 video sequences and evaluate on a separate set of 199 unseen sequences across all 13 animal categories. We construct batches of 32 sequences with 48 frames per sequence. We zero-pad the inputs up to the maximum of 29 joints that occur in dataset. We choose a layer size of 4 for the motion encoder and 12 for the space encoder. The hidden-dimension size D is 256. Experiments were conducted on a single NVIDIA A100 GPU.

MotionBERT uses human-specific semantic knowledge, making it unsuited for object-agnostic lifting. To provide a

fair comparison, we do not modify the proposed architecture and instead apply two other alterations. We first set the amount of learned positional embeddings to the maximum amount of joints seen in the dataset, allowing it to handle all animal rigs. We also randomly permute the 2D inputs during training and testing to simulate a real the object-agnostic scenario. This is required so that the positional embeddings are not learning dataset-specific skeleton semantics. We ensure that joints are permuted the same for a video sequence such that there remains temporal correspondence.

4.1. Object-agnostic lifting

Tab. 1 demonstrates the effectiveness of our method compared to both MotionBERT and 3D-LFM. We outperform both methods across all three metrics and nearly every animal. Notably, our approach achieves 45% lower SA-MPJPE and 70% lower SA-MPVE compared to 3D-LFM, demonstrating that our predicted 3D motion has both higher accuracy and smoother movement, while also preserving accurate structure (FA-MPJPE). This substantial performance gap highlights the critical role of the motion encoder in capturing the temporal relationship between joints. While MotionBERT is a spatio-temporal approach, it has no inductive bias to assist with handling scarce data and multi-category training. Fig. 3 qualitatively demonstrates the predictions of our method compared to 3D-LFM.

Single- vs multi-category We evaluate the performance of each method on single-category training and compare it to their performance on multi-category training in Sec. 4.1. For the single-category training, we train each approach from scratch using data specific to one animal category. This process is repeated for all 13 animals, and the mean error is reported in Tab. 2. All methods show significant improvement from multi-category training, achieving at least a 25% reduction in FA-MPJPE, with our approach achieving a 50% reduction. This improvement highlights the advantage of unified learning across a vast spectrum of object

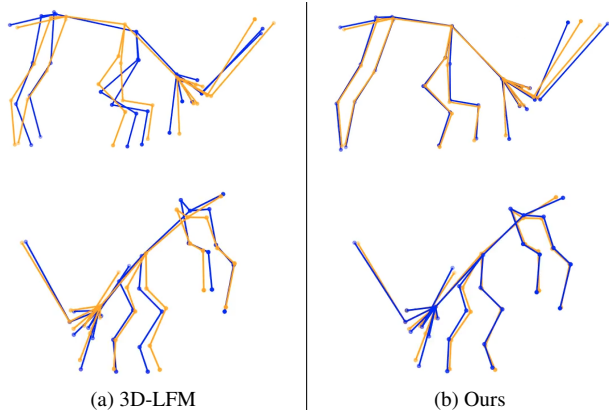


Figure 3. **Quantitative comparison on a *Deer* sequence from two different views:** Our method provides significantly more accurate 3D predictions. In this visualization, blue represents the predicted 3D points whereas the orange denotes the ground truth.

categories, particularly in scenarios where the training data is small and unbalanced.

Robustness to occlusion To evaluate the robustness of 3D-LFM and our approach to occlusion scenarios, we trained both models by randomly masking 10% of all 2D keypoints within a frame and tasking the models with recovering the 3D locations of the missing joints. As shown in Fig. 6a with 10% occlusion, our method demonstrates superior robustness to occlusions while 3D-LFM struggles. Even at an extreme case of 60% occlusion we continue to see legible predictions from our method, see supp. material for a qualitative result.

4.2. OOD generalization

Unseen objects We perform a 13-fold analysis, where each fold involves holding out one animal category from the original dataset during training. For example, in 1-fold, the *bunny* category is excluded from the training data and used to evaluate the generalisation capability of each method. As shown in Fig. 4 (left), our approach demonstrates superior OOD generalization when handling unseen animal categories by outperforming existing methods by a significant margin. We present a qualitative reconstruction for a *bunny* instance in Fig. 5 and refer the reader to the supp. material for tabulated results.

Rig transfer When lifting an unseen animal in the wild, we may encounter an animal with a more complex structure than seen during training. We showcase our ability to generalize to an unseen animal with an unseen number of joints. While MotionBERT is limited to rigs with the same or fewer joints as those seen during training, our method can handle *any* number of joints. We train on animal rigs with

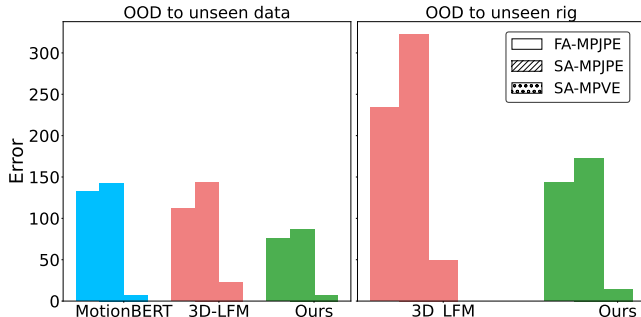


Figure 4. **OOD generalization.** *OOD to unseen data* (left): We perform a 13-fold evaluation to assess each method’s ability to handle unseen animal categories. *OOD to an unseen category and rig* (right): Note that MotionBERT is constrained to rigs with the same or fewer joints as those seen during training and hence cannot handle unseen rigs with more joints. Our method can handle generalization to both unseen category and unseen rig more effectively.

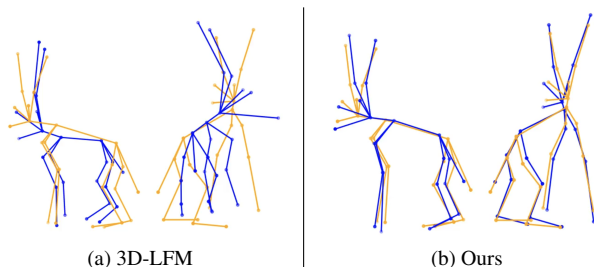


Figure 5. **OOD generalization on an unseen *Bunny* category from two different views:** Our method provides significantly more accurate 3D predictions compared to 3D-LFM. In this visualization, blue represents the predicted 3D points whereas the orange denotes the ground truth.

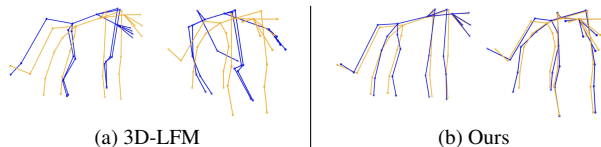


Figure 6. **A comparison of robustness when 10% of a tiger is occluded.** We include the average frame-aligned MPJPE across all animals for each method. Two views of the object are shown.

27 or fewer joints and test on two *unseen* animals with 29 joints (deer and moose). As shown in Fig. 4 (right), while both 3D-LFM and our approach are impacted by the difficulty of the task. Our approach outperforms 3D-LFM by at least 40% in all metrics. We show the tabulated results in the supp. material.

Model	FA-MPJPE↓	SA-MPJPE↓	SA-MPVE↓
Space	67.8	99.9	13.1
Time	57.9	66.5	5.6

Table 3. Ablation of time vs. space.

α	FA-MPJPE ↓	SA-MPJPE ↓	SA-MPVE ↓
2	53.9 \pm 1.12	65.5 \pm 0.96	7.0 \pm 0.02
4	54.4 \pm 1.13	64.9 \pm 2.78	6.4 \pm 0.01
8	52.7 \pm 0.19	61.4 \pm 0.40	5.8 \pm 0.00
16	57.1 \pm 0.93	65.6 \pm 1.70	5.7 \pm 0.02
-	57.9 \pm 0.33	66.5 \pm 0.88	5.6 \pm 0.01

Table 4. **Ablation of our inductive bias.** We use – to denote no constraint being applied. We report the averages over 5 independent runs.

4.3. Ablations

In this section we ablate the important building blocks of our approach. We first highlight the importance of our spatio-temporal approach as opposed to a spatial-only approach. Then, we demonstrate the improvement gained from our temporal-proximity inductive bias. We go on to compare strategies for encoding the position of a joint in time. Lastly, we ablate the importance of our procrustes-based training.

Time vs. space We evaluate the significance of information sharing across time facilitated by our proposed motion encoder. To isolate the impact of time, we create a space-only variant of our model by replacing the motion encoder with additional space blocks such that the number of parameters remains similar. As shown in Tab. 3, modelling temporal dependencies is crucial for enhancing 2D-3D lifting performance, particularly in terms of per-sequence reconstruction accuracy (SA-MPJPE) and smoothness (SA-MPVE).

Constrained temporal attention We observe that applying our inductive bias to restrict information sharing enhances the optimization of our model. We conduct our ablation by starting from having a strong inductive bias ($\alpha = 2$) inductive bias and progressively increasing it by a factor of 2. We do this until α is large enough to allow information sharing across the entire sequence ($\alpha = -$). We apply α according to Eq. (7). Tab. 4 shows the impact of different α on performance, averaged over five statistical runs. Overall, we observe a trade-off between the accuracy of the 3D structure and the accuracy of 3D motion. In our case we identify $\alpha = 8$ as optimal in our case, which we used for all of our experiments.

Temporal Embedding	FA-MPJPE↓	SA-MPJPE↓	SA-MPVE↓
-	55.5 \pm 2.29	64.8 \pm 3.04	5.9 \pm 0.03
Learned	54.0 \pm 1.13	64.1 \pm 1.24	6.1 \pm 0.02
Analytical	52.7 \pm 0.25	61.4 \pm 0.27	5.8 \pm 0.01

Table 5. **Ablation of temporal embedding strategies.** We report the averages over 5 independent runs.

Model	Procrustes	FA-MPJPE↓	SA-MPJPE↓	SA-MPVE↓
3D-LFM	-	83.2	97.3	25.0
3D-LFM	✓	68.3	108.7	18.0
Ours	-	62.2	74.9	7.7
Ours	✓	52.7	61.4	5.6

Table 6. **Procrustes vs. non-Procrustes-based training.** Our spatio-temporal 2D-3D lifting approach with Procrustean alignment surpasses 3D-LFM.

Analytical temporal embedding Here we ablate our use of our analytical RFF for encoding temporal information. In Tab. 5 we show that in our experiments it is beneficial to use an analytical embedding over a learned embedding. This embedding is important for the motion encoder to understand the ordering of frames in a sequence.

Procrustes-based training Similar to 3D-LFM, we find it useful to train our model with a Procrustes-based loss (PBL), as shown in Tab. 6. Allowing the model to focus on learning object structures significantly enhances the predicted 3D structure and benefits overall 3D motion accuracy. Interestingly, we observe that we are able to perform well without the PBL, even outperforming 3D-LFM across all metrics. This offers an interesting insight into future work with our method for practical applications that require implicitly predicted camera rotation.

5. Conclusion

In this work, we introduced an object-agnostic 3D lifting model that leverages a temporal inductive bias for temporal sequences. Our approach sets a new benchmark in lifting performance for object categories with limited available data. The model’s ability to generalize across unseen object categories and rigs shows its versatility and robustness, even in challenging scenarios involving noise and occlusions. In addition to these contributions, we have also introduced a new synthetic dataset designed to stimulate further research in class-agnostic 3D lifting models. This work paves the way for more generalized and efficient 3D reconstruction methods that can be applied across diverse real-world applications.

References

- [1] Liang An, Jilong Ren, Tao Yu, Tang Hai, Yichang Jia, and Yebin Liu. Three-dimensional surface motion capture of multiple freely moving pigs using MAMMAL. *Nature Communications*, 14(1):7727, 2023. 2
- [2] Ernesto Brau and Hao Jiang. 3D Human Pose Estimation via Deep Learning from 2D Annotations. In *2016 Fourth International Conference on 3D Vision (3DV)*, pages 582–591, 2016. 2, 1
- [3] Ju Yong Chang, Gyeongsik Moon, and Kyoung Mu Lee. PoseLifter: Absolute 3D human pose lifting network from a single noisy 2D human pose, 2020. 2
- [4] Tianlang Chen, Chen Fang, Xiaohui Shen, Yiheng Zhu, Zhili Chen, and Jiebo Luo. Anatomy-aware 3D Human Pose Estimation with Bone-based Pose Decomposition, 2021. 2, 5
- [5] Zheng Chen and Yi Sun. Joint-wise 2D to 3D lifting for hand pose estimation from a single RGB image. *Applied Intelligence*, 53(6):6421–6431, 2023. 2
- [6] Chaoqun Cheng, Zijian Huang, Ruiming Zhang, Guozheng Huang, Han Wang, Likai Tang, and Xiaoqin Wang. Marmose-Pose: A Deep Learning-Based System for Real-time Multi-Marmoset 3D Pose Tracking, 2024. 2
- [7] Mosam Dabhi, Laszlo A. Jeni, and Simon Lucey. 3D-LFM: Lifting Foundation Model, 2024. 1, 2, 4, 5
- [8] Carl Doersch, Ankush Gupta, Larisa Markeeva, Adrià Recasens, Lucas Smaira, Yusuf Aytar, João Carreira, Andrew Zisserman, and Yi Yang. TAP-Vid: A Benchmark for Tracking Any Point in a Video, 2023. 2
- [9] Lihao Ge, Zhou Ren, Yuncheng Li, Zehao Xue, Yingying Wang, Jianfei Cai, and Junsong Yuan. 3D Hand Shape and Pose Estimation from a Single RGB Image, 2019. 2
- [10] Adam Gosztołai, Semih Günel, Marco Pietro Abrate, Daniel Morales, Victor Lobato Ríos, Helge Rhodin, Pascal Fua, and Pavan Ramdya. LiftPose3D, a deep learning-based approach for transforming 2D to 3D pose in laboratory animals, 2020. 2
- [11] Mir Rayat Imtiaz Hossain and James J. Little. Exploiting Temporal Information for 3D Human Pose Estimation. In *Computer Vision – ECCV 2018*, pages 69–86. Springer International Publishing, Cham, 2018. 2, 5
- [12] Catalin Ionescu, Dragos Papava, Vlad Olaru, and Cristian Sminchisescu. Human3.6M: Large Scale Datasets and Predictive Methods for 3D Human Sensing in Natural Environments. *IEEE Transactions on Pattern Analysis and Machine Intelligence*, 36(7):1325–1339, 2014. 1
- [13] Haorui Ji, Hui Deng, Yuchao Dai, and Hongdong Li. Unsupervised 3D Pose Estimation with Non-Rigid Structure-from-Motion Modeling, 2023. 2
- [14] Nikita Karaev, Ignacio Rocco, Benjamin Graham, Natalia Neverova, Andrea Vedaldi, and Christian Rupprecht. DynamicStereo: Consistent Dynamic Depth from Stereo Videos. In *2023 IEEE/CVF Conference on Computer Vision and Pattern Recognition (CVPR)*, pages 13229–13239, Vancouver, BC, Canada, 2023. IEEE. 2
- [15] Pierre Karashchuk, Katie L. Rupp, Eryn S. Dickinson, Sarah Walling-Bell, Elischa Sanders, Eiman Azim, Bingni W. Brunton, and John C. Tuthill. Anipose: A toolkit for robust markerless 3D pose estimation. *Cell Reports*, 36(13), 2021. 2
- [16] Diederik P. Kingma and Jimmy Ba. Adam: A Method for Stochastic Optimization, 2017. 1
- [17] Chen Kong and Simon Lucey. Deep Non-Rigid Structure From Motion. In *2019 IEEE/CVF International Conference on Computer Vision (ICCV)*, pages 1558–1567, Seoul, Korea (South), 2019. IEEE. 2
- [18] Ci Li, Ylva Mellbin, Johanna Krogager, Senya Polikovsky, Martin Holmberg, Nima Ghorbani, Michael J. Black, Hedvig Kjellström, Silvia Zuffi, and Elin Hernlund. The Poses for Equine Research Dataset (PFERD). *Scientific Data*, 11(1): 497, 2024. 2
- [19] Yang Li, Hikari Takehara, Takafumi Taketomi, Bo Zheng, and Matthias Nießner. 4DComplete: Non-Rigid Motion Estimation Beyond the Observable Surface. <https://arxiv.org/abs/2105.01905v1>, 2021. 2, 3
- [20] Ruixu Liu, Ju Shen, He Wang, Chen Chen, Sen-ching Cheng, and Vijayan Asari. Attention Mechanism Exploits Temporal Contexts: Real-Time 3D Human Pose Reconstruction. In *2020 IEEE/CVF Conference on Computer Vision and Pattern Recognition (CVPR)*, pages 5063–5072, Seattle, WA, USA, 2020. IEEE. 2, 5
- [21] Alexander Mathis, Pranav Mamidanna, Taiga Abe, Kevin M. Cury, Venkatesh N. Murthy, Mackenzie W. Mathis, and Matthias Bethge. Markerless tracking of user-defined features with deep learning, 2018. 2
- [22] Gyeongsik Moon, Ju Yong Chang, and Kyoung Mu Lee. Camera Distance-aware Top-down Approach for 3D Multi-person Pose Estimation from a Single RGB Image, 2019. 2
- [23] Alejandro Newell, Kaiyu Yang, and Jia Deng. Stacked Hourglass Networks for Human Pose Estimation, 2016. 1
- [24] David Novotny, Nikhila Ravi, Benjamin Graham, Natalia Neverova, and Andrea Vedaldi. C3DPO: Canonical 3D Pose Networks for Non-Rigid Structure From Motion, 2019. 2
- [25] Sunghoon Park, Jihye Hwang, and Nojun Kwak. 3D Human Pose Estimation Using Convolutional Neural Networks with 2D Pose Information, 2016. 2
- [26] Georgios Pavlakos, Xiaowei Zhou, and Kostas Daniilidis. Ordinal Depth Supervision for 3D Human Pose Estimation, 2018. 2
- [27] Fabian Plum, René Bulla, Hendrik K. Beck, Natalie Imirzian, and David Labonte. replicAnt: A pipeline for generating annotated images of animals in complex environments using Unreal Engine. *Nature Communications*, 14(1): 7195, 2023. 2
- [28] Chaoyang Wang and Simon Lucey. PAUL: Procrustean Autoencoder for Unsupervised Lifting. In *2021 IEEE/CVF Conference on Computer Vision and Pattern Recognition (CVPR)*, pages 434–443, Nashville, TN, USA, 2021. IEEE. 2
- [29] Jiacong Xu, Yi Zhang, Jiawei Peng, Wufei Ma, Artur Jesslen, Pengliang Ji, Qixin Hu, Jiehua Zhang, Qihao Liu, Jiahao Wang, Wei Ji, Chen Wang, Xiaoding Yuan, Prakhar Kaushik, Guofeng Zhang, Jie Liu, Yushan Xie, Yawen Cui, Alan Yuille, and Adam Kortylewski. Animal3D: A Comprehensive Dataset of 3D Animal Pose and Shape, 2024. 2

- [30] Yufei Xu, Jing Zhang, Qiming Zhang, and Dacheng Tao. ViTPose: Simple Vision Transformer Baselines for Human Pose Estimation, 2022. [5](#)
- [31] Yuan Yao, Praneet Bala, Abhiraj Mohan, Eliza Bliss-Moreau, Kristine Coleman, Sienna M. Freeman, Christopher J. Machado, Jessica Raper, Jan Zimmermann, Benjamin Y. Hayden, and Hyun Soo Park. OpenMonkeyChallenge: Dataset and Benchmark Challenges for Pose Estimation of Non-human Primates. *International journal of computer vision*, 131(1):243–258, 2023. [2](#)
- [32] Jianqiao Zheng, Xueqian Li, Sameera Ramasinghe, and Simon Lucey. Robust Point Cloud Processing through Positional Embedding, 2023. [4](#)
- [33] Yang Zheng, Adam W. Harley, Bokui Shen, Gordon Wetstein, and Leonidas J. Guibas. PointOdyssey: A Large-Scale Synthetic Dataset for Long-Term Point Tracking, 2023. [2](#)
- [34] Wentao Zhu, Xiaoxuan Ma, Zhaoyang Liu, Libin Liu, Wayne Wu, and Yizhou Wang. MotionBERT: A Unified Perspective on Learning Human Motion Representations, 2023. [1](#), [2](#), [5](#)

Object Agnostic 3D Lifting in Space and Time

Supplementary Material

A. Extra training details

We train our model with the Adam [16] optimizer using $\text{lr} = 10^{-4}$, weight decay of 10^{-6} , $\beta_1 = 0.9$, and $\beta_2 = 0.999$. We set the velocity loss term $\lambda = 5000$. We train for a total of 1000 epochs and use the model with the lowest validation error out of all epochs.

B. Dataset details

B.1. Statistics

An overview of our dataset can be seen in Tab. 7. We showcase the number of joints, animations, and frames for each animal category. Our dataset contains a variety of different categories and rigs to facilitate class-agnostic training and evaluation.

B.2. Examples

We provide an additional **dataset_examples.mp4** video in the supplementary zip file for viewing the 3D skeletons for some animals.

C. Additional results

C.1. Examples

We provide an additional **prediction_examples.mp4** video in the supplementary zip file for viewing some predictions over a series of video sequences. We provide a side-by-side comparison between our approach and 3D-LFM. We also provide examples of out-of-distribution predictions. We believe that these videos provide a more comprehensive comparison than that which can be obtained with 2D images.

C.2. Ablating 2D noise

Alongside Tab. 1 in the main paper, we provide additional experiments on our dataset where we do not apply synthetic noise to the 2D inputs. Tab. 8 shows that the improvements provided by our approach over existing methods is not restricted to situations with noisy 2D poses.

C.3. Human3.6M benchmark

We provide comparisons on the Human3.6M [12] benchmark containing 3.6 million video frames of real humans performing simple tasks in a controlled indoor environment. Following previous lifting works [2, 34], we train on subjects 1, 5, 6, 7, and 8, and hold out subjects 9 and 11 for testing. We use the noisy 2D skeletons provided by [34] that were obtained using Stacked Hourglass Networks [23]. Every fifth frame is used for all experiments

with no significant degradation in performance. We additionally compare with the original MotionBERT [34], denoted with \dagger in Tab. 11, that uses human-specific augmentation during training and human-specific semantic correspondences. We find that, when there is an abundance of data for a single object, leveraging object-specific information is preferred to class-agnostic training. Tab. 11 further demonstrates the benefit of our approach over the current SOTA class-agnostic method [7]. We outperform 3D-LFM on each metric, translating to improved 3D object structure and motion consistency across entire sequences. The class-agnostic MotionBERT outperforms both our approach and 3D-LFM, likely due to the having twice as many parameters and an architecture that was specifically designed for large-scale human data.

C.4. Per-animal multi-category

Here we provide the per-animal results that correspond to Tab. 2 in the main paper. Tab. 12 demonstrates the usefulness of training with all categories at once instead of specializing to a single category. We find that this holds true for our model across all animal categories. The same is seen for MotionBERT and 3D-LFM with exception of the chicken category, where it is sometimes slightly better to do chicken-only training.

C.5. Out-of-distribution categories and rigs

Here we provide tabulated results for our out-of-distribution (OOD) experiments found in Sec. 4.2 in the main paper. We show in Tabs. 9 and 10 that our model does indeed maintain superior OOD performance across all metrics compared to existing methods. In the case of unseen number of joints (Tab. 10), we cannot evaluate MotionBERT as it is unable to handle a number of joints that is more than the maximum seen during training.

C.6. Extreme occlusion

We provide a visual comparison between our approach and 3D-LFM when there is an extreme (60%) occlusion of the object. Fig. 7 demonstrates the robustness of our approach in this scenario. While 3D-LFM fails to properly reconstruct the 3D object structure (Fig. 7a) for even a single frame, our method is capable of maintaining high-fidelity reconstruction (Fig. 7b). We show FA-MPJPE results for intermediate occlusion levels in Fig. 8.

	Bear	Buck	Bunny	Chicken	Deer	Dog	Elk	Fox	Moose	Puma	Rabbit	Raccoon	Tiger	Total
Animations	67	42	45	7	56	65	67	37	59	68	45	54	66	678
Frames	4,464	3,168	3,072	432	3,648	4,128	5,328	2,304	3,792	5,808	3,072	4,176	4,992	48,384
Joints	21	27	25	19	29	22	26	26	29	26	25	28	27	330

Table 7. **An overview of our synthetic dataset.** We measure the total number of animation sequences and frames for each animal. We also provide the number of joints that constitute each animal.

Method	Bear	Buck	Bunny	Chicken	Deer	Dog	Elk	Fox	Moose	Puma	Rabbit	Raccoon	Tiger	Avg
MotionBERT	94.9	216.1	17.7	110.7	198.4	49.1	233.1	38.0	161.8	257.4	28.1	83.1	220.8	131.5
3D-LFM	49.8	151.2	23.8	106.7	151.3	53.6	149.8	21.5	277.0	157.4	40.4	62.3	162.9	108.0
Ours	28.7	125.4	15.8	80.4	59.4	31.6	122.4	13.7	98.2	93.7	17.6	45.4	93.1	63.5

MotionBERT	90.9	205.3	17.0	98.6	189.9	45.7	211.7	36.4	143.3	237.5	26.3	80.7	210.9	122.6
3D-LFM	31.3	100.4	12.7	97.6	67.4	33.8	104.4	15.3	113.5	114.3	26.4	49.6	107.1	67.1
Ours	26.3	108.9	10.6	70.5	52.8	26.2	98.6	11.8	78.6	87.6	15.1	43.9	81.6	54.8

MotionBERT	2.6	9.1	0.9	3.9	7.1	2.0	9.4	1.2	13.0	9.1	1.8	3.4	8.5	5.5
3D-LFM	5.3	18.5	2.3	5.7	14.1	5.2	13.8	2.3	32.3	17.0	4.8	6.6	18.9	11.6
Ours	2.2	10.1	1.2	4.2	5.0	2.5	10.8	1.0	12.6	7.8	1.7	3.1	8.7	5.4

Table 8. **Quantitative comparison when no artificial noise is applied to the 2D keypoints.** We report, in millimeters, the Sequence-Aligned MPJPE (top), Frame-Aligned MPJPE (middle), and Sequence-Aligned MPVE (bottom). Our approach (Ours) consistently outperforms existing methods across all metrics.

Method	FA-MPJPE ↓	SA-MPJPE ↓	SA-MPVE ↓
MotionBERT	132.0	142.5	6.8
3D-LFM	112.0	143.4	21.9
Ours	75.7	86.4	6.4

Table 9. **OOD generalization on unseen data.** We perform a 13-fold evaluation to assess each method’s ability to handle unseen animal categories. Our approach demonstrates superior proficiency in handling OOD 2D-3D lifting.

Method	FA-MPJPE ↓	SA-MPJPE ↓	SA-MPVE ↓
3D-LFM	234.4	321.7	49.0
Ours	143.0	172.9	14.5

Table 10. **OOD generalization on unseen category and rig.** Models are trained on rigs with 28 or less joints and evaluated on unseen deer and moose categories with 29 joints.

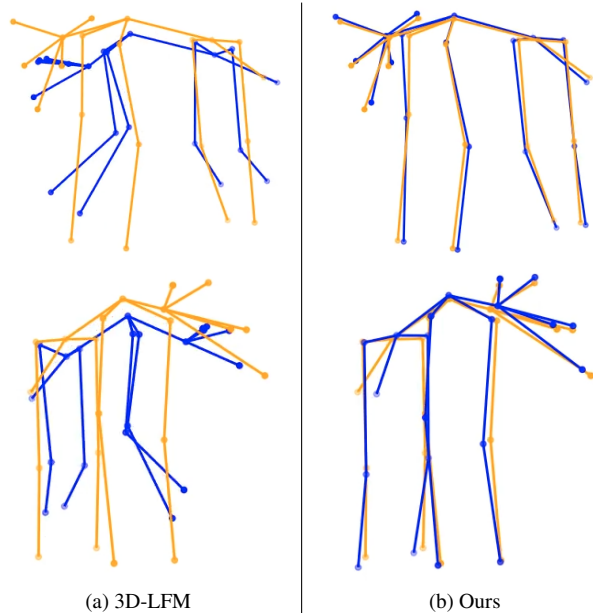


Figure 7. **A comparison of robustness in an extreme case of 60% occlusion.** We showcase the predictions for a bear at 2 different views. Ground truth is orange, prediction is blue.

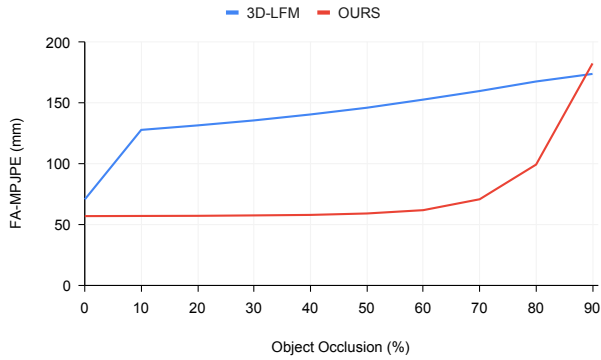


Figure 8. **A comparison of robustness at increasing levels of object occlusion.** Our approach maintains high-fidelity 3D reconstruction, even at extreme levels of occlusion.

Method	FA-MPJPE↓	SA-MPJPE↓	SA-MPVE↓
MotionBERT†	34.8	37.2	8.8
MotionBERT	39.3	41.8	9.1
3D-LFM	48.4	63.2	29.8
Ours	42.9	49.0	11.1

Table 11. **Results on the Human3.6M benchmark.** MotionBERT† is the original human-specific model. MotionBERT has twice as many parameters and is designed for large-scale human data, while we are designed for small-scale multi-object data.

Method	MC	Bear	Buck	Bunny	Chicken	Deer	Dog	Elk	Fox	Moose	Puma	Rabbit	Raccoon	Tiger	Avg
MotionBERT	-	142.1	315.5	36.4	110.0	297.5	108.0	293.1	70.9	381.6	288.1	94.2	107.5	353.7	199.9
	✓	94.5	208.1	16.7	108.2	200.7	50.1	267.4	40.6	189.2	254.4	30.7	77.4	211.8	134.6
3D-LFM	-	58.1	183.3	24.1	101.3	192.2	63.7	168.9	25.2	316.6	187.8	43.1	79.1	199.3	126.4
	✓	47.6	158.2	23.2	92.3	156.8	53.9	147.8	22.2	274.7	163.4	37.8	70.0	165.4	108.7
Ours	-	70.4	205.9	22.7	94.4	152.2	78.8	193.0	38.7	271.5	158.0	47.0	67.6	269.0	128.4
	✓	29.2	128.4	17.1	60.8	57.3	32.8	103.1	14.2	97.9	93.2	19.0	44.5	90.8	60.6
MotionBERT	-	127.5	285.0	30.6	96.4	264.4	90.9	263.0	63.8	305.9	258.4	93.6	98.4	309.6	176.0
	✓	90.7	198.1	16.0	99.0	195.5	45.8	246.8	39.9	170.9	235.0	28.6	74.9	203.2	126.5
3D-LFM	-	38.9	138.3	13.7	89.9	115.3	45.7	123.9	21.0	177.9	152.5	27.0	67.3	148.4	89.2
	✓	27.9	108.3	12.2	86.3	75.0	33.3	103.0	16.2	119.7	119.3	21.2	57.6	107.7	68.3
Ours	-	63.1	168.5	16.9	85.0	130.1	56.1	158.3	35.1	202.1	142.5	34.8	60.0	217.2	105.4
	✓	26.7	107.3	11.2	54.2	50.9	27.9	86.1	12.4	81.6	85.9	15.4	42.8	79.8	52.5
MotionBERT	-	5.0	16.9	2.2	3.4	12.6	5.3	12.7	2.3	26.9	12.6	4.8	5.7	16.8	9.8
	✓	3.2	11.0	1.1	3.9	6.9	2.6	10.4	1.3	17.8	9.8	2.1	4.0	9.8	6.5
3D-LFM	-	11.3	37.3	4.0	3.6	30.9	10.3	29.7	4.8	51.4	29.7	7.1	13.2	32.6	20.5
	✓	7.6	29.0	3.4	8.4	26.3	8.4	26.5	3.8	43.4	27.3	6.7	12.3	30.4	18.0
Ours	-	6.4	19.3	2.4	4.3	13.4	7.1	14.7	2.2	28.2	13.2	5.4	5.9	20.4	11.0
	✓	2.5	12.1	1.3	3.4	5.9	2.9	9.3	1.2	12.5	8.9	2.0	3.6	9.1	5.7

Table 12. **Per-animal comparison of multi-category and single-category training.** We use a ✓ for models trained with multiple categories (MC). We report, in millimeters, the Sequence-Aligned MPJPE (top), Frame-Aligned MPJPE (middle), and Sequence-Aligned MPVE (bottom). Top, middle, and bottom are separated by dual horizontal lines.